Electrocatalysis (2017) 8:16–26
DOI 10.1007/s12678-016-0336-8

ORIGINAL RESEARCH

Concurrent Deposition and Exfoliation of Nickel Hydroxide Nanoflakes Using Liquid Crystal Template and Their Activity for Urea Electrooxidation in Alkaline Medium

Mohamed A. Ghanem[1,2] · **Abdullah M. Al-Mayouf**[1] · **Jai P. Singh**[1] · **Prabhakarn Arunachalam**[1]

Published online: 22 October 2016

Abstract Nickel hydroxide nanoflakes ($Ni(OH)_2$-NF) were prepared by chemical deposition and in situ exfoliation of nickel hydroxide layers confined in the aqueous domain of the liquid crystalline hexagonal template of Brij®78 surfactant. Using excess of sodium borohydride as a reducing agent generates concurrent excessive dynamic hydrogen bubbles which exfoliated and fragmented the nickel hydroxide layers precipitated within the soft hexagonal template. The physicochemical characterizations of $Ni(OH)_2$-NF by using surface area analyser, X-ray diffraction (XRD), XPS and transmission electron microscope (TEM) showed the formation of α-$Ni(OH)_2$ nanoflakes with thickness of 2–3 nm and have about 450 $m^2\ g^{-1}$ surface area which is 20 times higher than that for bare nickel (bare-Ni) deposited without surfactant template. The electrocatalytic activity of the $Ni(OH)_2$-NF catalyst for urea electrolysis was studied by cyclic voltammetry and chronoamperometry techniques. The $Ni(OH)_2$-NF has shown a superior activity for the electrochemical oxidation of urea in alkaline solution and exhibits more than tenfold increase in activity in comparison with the bare-Ni deposit. The enhancement of urea electrooxidation activity was related to the superficial enhancement in the electroactive surface area of $Ni(OH)_2$-NF. This new approach of deposition and in situ exfoliation by using liquid crystal template and hydrogen bubbles offers a new platform to nanostructuring wide range of catalysts with better catalytic performance.

✉ Mohamed A. Ghanem
mghanem@ksu.edu.sa

[1] Electrochemistry Research Group, Chemistry Department, College of Science, King Saud University, Riyadh 11451, Saudi Arabia

[2] Faculty of Petroleum and Mining Engineering, Suez University, Suez, Egypt

Keywords Nickel hydroxide · Nanoflakes · Liquid crystal template · Electrooxidation · Urea

Introduction

The increasing in worldwide energy demands has led to search for alternative clean energy sources other than fossil fuels. Hydrogen fuel is a long-term sustainable energy source and commonly produced by natural gas reforming and water electrolysis [1–3]. Recently, more attention has been directed to use ammonia or urea containing wastewater as sources for hydrogen production by electrolysis [4–7]. Up to 0.3 M of urea is available in wastewater, and the electrolysis of urea-containing wastewater has become a very beneficial method. Electrolysis not only eliminates the urea or ammonia from wastewater providing non-toxic products such as CO_2 and N_2 at the anode but also yields valuable hydrogen gas at the cathode [8, 9].

An inexpensive catalysts such as nickel-based compounds are effective and stable electrocatalysts for the oxidation of small organic molecules as well as for the electrolysis of urea in alkaline medium [10–13]. These conventional nickel-based catalysts have been extensively investigated for an electrooxidation of urea [5, 14], and substantial knowledge about the activity and the reaction mechanism has already been documented.

In alkaline solution, the electrochemical oxidation process of urea follows the mechanism of catalyst regeneration where divalent $Ni(OH)_2$ is electrochemically oxidized to trivalent NiOOH which, in turn, catalyse the urea oxidation reaction. It is documented that urea is oxidized at anodic potential of −0.46 V while the water reduction potential at the cathode occurs at −0.83 V vs. RHE in alkaline solution. Consequently, at the standard conditions, the thermodynamic

potential required to electrolyse urea is equal to 0.37 V [5] which is considerably lower than 1.23 V, the potential required for water electrolysis. Therefore, by using urea electrolysis, about 70 % cheaper hydrogen can be produced in addition to wastewater treatment and more hydrogen production at the cathode [4, 15].

The material nanostructuring by exfoliation and fragmentation of the layered structures becomes more attractive approach to produce (2D) nanosheets with molecular-scale thickness for catalysis and energy applications [16–18]. Nanostructured 2D nanosheets of transition metal hydroxides and oxides are obtained by microwave-assisted liquid-phase growth [19], hydrothermal surfactant exfoliating layers [20–22] and lithiation/delithiation process [23]. The distinctive structure property of high surface atoms ratio, efficient active sites and short ion and electron diffusion path significantly improved the electrochemical activity and supercapacitance performance of these nanosheet structures. Template method also has opened a new field of producing new architectures of nanostructured and mesoporous materials with high surface area, open mesoporous structures and uniform pore diameters which exhibit enhanced catalytic activity. Using this approach, Bartlett et al. [24, 25] established synthesis approach for mesoporous metal films by using the electrochemical reduction of the metal ions confined in the aqueous domain of the hexagonal liquid crystal templates. In relevant work, Osaka et al. reported the synthesis of highly ordered mesoporous nickel [26] and nickel–cobalt powders [27] by chemical reduction by using liquid crystal templates without investigating the electrochemical reactivity of these nanostructured materials. Also, mesoporous α-$Ni(OH)_2$ having a surface area of 230 $m^2\ g^{-1}$ was produced by chemical precipitation of Ni(II) ions with NaOH in the presence of cetyltrimethylammonium bromide micelles. The mesoporous α-$Ni(OH)_2$ structure demonstrates an excellent electrochemical performance as a cathode for alkaline nickel-based battery [28]. In recent work by our group, mesoporous Ni/$Ni(OH)_2$ catalyst was prepared by chemical reduction by using lyotropic surfactant template, and the catalyst shows a very significant electrocatalytic performance for ethanol oxidation [29]. The electrochemical activity for ethanol oxidation reached up to 10 times higher than bare nickel prepared in the absence of surfactant. This was attributed to the formation of mesoporous network with a large active surface area that permits effective ion mass transport and forms larger catalyst/solution interface. However, during the chemical reduction process, the concurrent evolved hydrogen damaged the pores' order of mesoporous structure. In addition, the mesoporous nickel framework was highly oxidized to $Ni(OH)_2$. In continuing of this research, here, we show a facile template chemical synthesis of α-$Ni(OH)_2$ nanoflakes ($Ni(OH)_2$-NF) with high surface area (470 $m^2\ g^{-1}$) and ultrathin 2D layers by using in situ chemical reduction and exfoliation of nickel ions confined in the aqueous domain of surfactant template. In this approach, it is intended to use excess of $NaBH_4$ as a reducing agent to produced excessive hydrogen gas bubbles which in situ exfoliate the nickel hydroxide layers precipitated within the aqueous domain of the hexagonal template of Brij®78 surfactant. The $Ni(OH)_2$-NF is characterized by X-ray diffraction (XRD), XPS, surface area analyser, transmission electron microscope (TEM) and electrochemical measurements. The electrochemical behaviour and activity of the $Ni(OH)_2$-NF for electrooxidation of urea in alkaline media are investigated and compared with bulk nickel catalyst deposited in the absence of surfactant.

Experimental

The chemicals used in this work were of analytical reagent and were used as received without any additional purification. All aqueous solutions were prepared by using Millipore ultrapure water (18.2 MΩ cm) purified by the Milli-Q (Millipore, Inc.) system. $Ni(OH)_2$-NF were prepared according to a modified procedure recently reported by our group [29]. Concisely, nickel(II) acetate (0.65 g, 2.6×10^{-3} mol) (Alfa Aesar, purity >97 %) was dissolved in deionized water (3.3 g). The nickel acetate solution was added into the melted non-ionic surfactant of Brij®78 ($C_{18}H_{37}(OCH_2CH_2)_{20}OH$, Aldrich, purity >97 %), and the ratio of surfactant was maintained at 55 wt%. The mixture was heated at 45 °C in a glass vial and manually mixed thoroughly by using glass rod. The complete mixing was assured as shown in Fig. 2a by the homogeneity of the green colour of formed liquid crystal template. The mixture was kept in sealed vial in the oven at 50 °C for 2 h, and the liquid crystal phase was examined by Meiji MT9930 microscope. For the deposition of nickel hydroxide nanoflakes, a solution of sodium borohydride reducing agent ($NaBH_4$, >97 %, Aldrich) (0.25 g, 6.7×10^{-3} mol) was dissolved in 2.0 ml deionized water then added drop by drop while mixing the template mixture. During the reduction process, the template mixture turns to black and vigorous hydrogen gas was observed. After lifted for overnight, the colour of the template mixture was completely turned to grey indicating the completion of reduction process. Then, the templates were removed by washing four to five times with 50 % isopropanol solution with distilled water, and finally, the mesoporous catalyst was collected by centrifugation and dried in the oven at 80 °C for overnight. For the sake of comparison, bare nickel (bare-Ni) was also prepared but in this case without surfactant and nickel(II) acetate solution was reduced by the same $NaBH_4$ reducing agent. Lastly, all as-prepared products were collected by the centrifuge method and dried into the oven at 80 °C for overnight.

Nickel hydroxide ink for electrochemical characterization was prepared by dispersing 4 mg of each catalyst by using probe sonication for 20 min in a mixture of 10 μl Nafion (5 wt%), 0.5 ml isopropanol and 0.5 ml deionized water. Then, for each

electrode, 10 μl (≅40 μg) of the ink was cast onto freshly polished glassy carbon disc (0.07 cm^2), and the solvent was dried at room temperature. GC electrode modified by the $Ni(OH)_2$ nanoflakes and bare nickel is nominated as $Ni(OH)_2$-NF and bare-Ni, respectively.

The fine structure of $Ni(OH)_2$-NF catalyst was examined with a TEM (Jeol JEOL-6330), and the crystal structure of the materials was measured by XRD (Rigaku D/MAX 2500). The surface area of the mesoporous powders was measured by the Brunauere–Emmett–Teller (BET) method by using a V-Sorb 2800 Porosimetry Analyser (Gold APP Instruments, China).

Conventional three-electrode single-compartment Pyrex glass cell was used for all the electrochemical measurements in a KOH solution, in the absence and presence of urea by using an Autolab II computerized potentiostate. A platinum foil (1 cm^2) and saturated calomel electrode (SCE) were employed as counter and reference electrodes, respectively. Newly prepared catalyst for each experiment was used, and each experiment was repeated at least three times.

Results and Discussion

For the characterization of nickel liquid crystal template, Fig. 1a shows the polarized light optical image of the nickel acetate template mixture where the texture of fan-like appearance is clearly observed under the polarized light. The template is highly viscous, and small air bubbles trapped within are obviously apparent. Figure 1b shows the low-angle XRD pattern recorded for the hexagonal structure of the nickel acetate template mixture. The low-angle XRD exhibits two diffraction peaks which can assign to the (100) and (110) diffraction planes of the hexagonal structure. The d-spacing of the (100) and (110) diffraction planes is 65 and 37 Å, respectively. The ratio between *d*-spacing of (100) and (110) diffraction planes is $1:1/\sqrt{3}$ which is in good agreement with that for hexagonal phase and confirms the formation of hexagonal liquid structure [24, 25, 29].

The normal topology of the surfactant hexagonal phase is the hydrocarbon chains that are contained within the cylindrical aggregates and water fills in the voids between the hexagonally packed cylinders. $Ni(OH)_2$-NF were prepared as shown in Scheme 1 by chemical reduction of nickel ions dissolved in the aqueous domain that confined between the hexagonal cylindrical of Brij®78 surfactant. Using excess of $NaBH_4$ as a reducing agent produces excessive dynamic hydrogen bubbles which concurrently exfoliated and fragmented the nickel hydroxide layers precipitated within the aqueous domain of the soft surfactant template.

Figure 2 shows the optical images for (a) the template mixture and (b) directly after mixing the template mixture with $NaBH_4$ reducing agent solution. Clearly, the template starts to swell due to hydrogen gas evolution and the green colour gradually turns to grey indicative on the initiation of nickel hydroxide deposition within the Brij®78 surfactant template. Evolution of hydrogen gas during the deposition process was continued, and a significant template swell was observed as shown in Fig. 2c. Nickel hydroxide nanoflakes powder (d) was obtained after washing the surfactant and drying the precipitate.

The morphology and fine structure of $Ni(OH)_2$-NF are firstly inspected by TEM characterization, and Fig. 3 shows the TEM images for the obtained $Ni(OH)_2$-NF at different magnification. The images clearly show flakes-like morphology that rolled up and wrinkling together. As shown in Fig. 3b, the flakes are highly transparent suggesting characteristic feature of ultrathin 2D sheets or flat-layer structures. Because the use of soft template and effervesce of hydrogen gas, the produced nickel hydroxide nanoflakes are highly irregular, crumbled and overlapped together which makes it is difficult to resolve their exact size. However, it can conclude the nanoflakes are few nanometres in size which is much smaller than a micron size of nickel hydroxide nanosheets obtained by microwave-assisted synthesis [19]. This could be associated to the size of the aqueous domain in the original hexagonal liquid crystal template. Also, because of the dynamic hydrogen evolution during the deposition process,

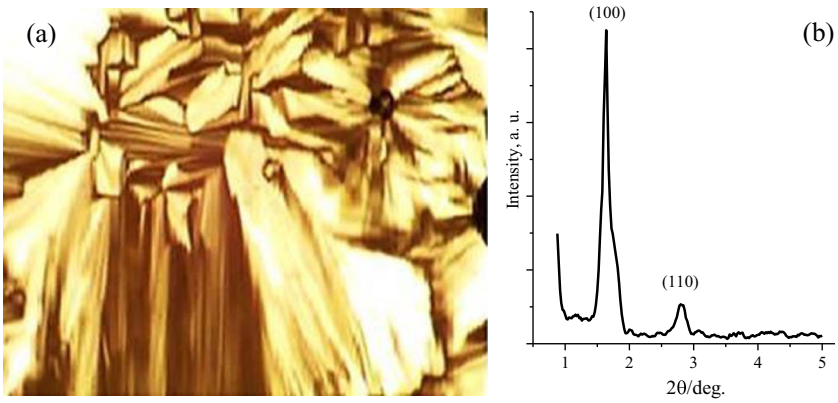

Fig. 1 **a** Polarized light optical images of the hexagonal nickel acetate template mixture. **b** Low-angle XRD for the nickel acetate template mixture

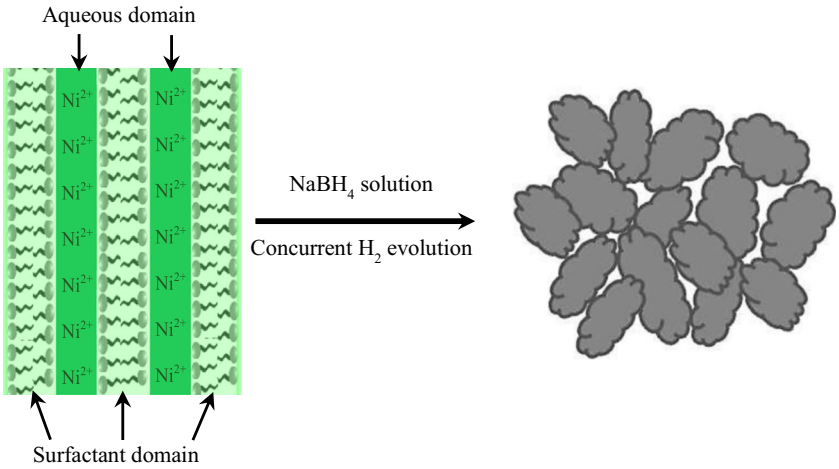

Scheme 1 Schematic illustration for the synthesis of $Ni(OH)_2$-NF via in situ chemical reduction and exfoliation using liquid crystal template

the nickel hydroxide structure is not expected to preserve the replica of the original hexagonal template, but lamellar 2D structures are likely. The thickness of the nanoflakes can be correlated to the thickness of the interstitial aqueous domain between the surfactant hexagonal columns and can be estimated at 2–3 nm thick as indicated by the arrow in TEM image in Fig. 3b. This is within the range of the reported value (≅3 nm) for the thickness of the interstitial aqueous domain for this type of surfactant [24, 25, 29].

In contrast for bare nickel, the TEM image in Fig. 3d shows dark area indicating on very thick layer of deposit with no evidence for the formation of nanoflakes as in the case of deposition in the presence of Brij®78 surfactant template. In relevant work, it is found that the hydrogen generation during the electroless deposition by using soft liquid crystal template greatly reduces the order of mesopores [26, 27], while slowing the deposition rate yields highly ordered hexagonal pores. Here by using an excess of $NaBH_4$ reducing agent, it is intended to increase the generation of hydrogen bubbles which act as a dynamic template and exfoliates the nickel hydroxide layers deposited within the hexagonal aqueous domain of liquid crystal template. The higher magnification TEM image in Fig. 3c depicts the amorphous structure of the $Ni(OH)_2$-NF with no preference diffraction pattern which is consistent with the X-ray diffraction result shown below.

Figure 4a displays the high-angle XRD pattern for the obtained $Ni(OH)_2$ nanoflakes. The X-ray diffraction peaks at 2θ = 10.85, 33.9 and 59.8 can be assigned to the diffraction planes of (001), (110) and (300), respectively, which are characteristic for hydrated form of α-$Ni(OH)_2$ (JCPDS 22-0444). The diffraction peak at 2θ = 44.50 can be assigned to Ni (111) diffraction plane. The X-ray diffraction peaks are broad which reveals small grain and amorphous structure, and the (110) diffraction peak of α-$Ni(OH)_2$ is asymmetric at the higher angle side indicating 2D structure with stacking defaults. The composition analysis of $Ni(OH)_2$-NF by using EDX analysis is presented in Fig. 4b, and clearly, only the lines for Ni-K, Ni-L and O-K are detected, which confirms the formation of nickel hydroxide deposit with no contaminations. The EDX composition analysis shows that the molar ratio of Ni/O is about 1.0:1.8 which is less than the stoichiometric ratio of 1:2 of α-$Ni(OH)_2$ and may be related to the presence of bulk nickel metal incorporated with α-$Ni(OH)_2$.

To gain more information about the chemical state and bonding configuration of nickel hydroxide nanoflakes, Fig. 5 shows the XPS characterization of the prepared $Ni(OH)_2$-NF. A usual survey of the XPS in Fig. 5a reveals the main photoelectron peaks corresponding to Ni 2p and O 1s with a very small peak for C 1s, which certifies the existence of nickel and oxygen with minor contamination of carbon.

Figure 5b shows the deconvolution details of the Ni 2p peak which display spin-orbit component corresponding to $2p_{3/2}$ and $2p_{1/2}$ peaks observed at 855.8 and 874.5 eV, respectively.

In addition, a satellite peak for $2p_{3/2}$ and $2p_{1/2}$ was also observed at 862.6 and 880.7, respectively. The XPS spectrum and shape shown in Fig. 5b is very consistence with the characteristic structure of nickel hydroxide ($Ni(OH)_2$)

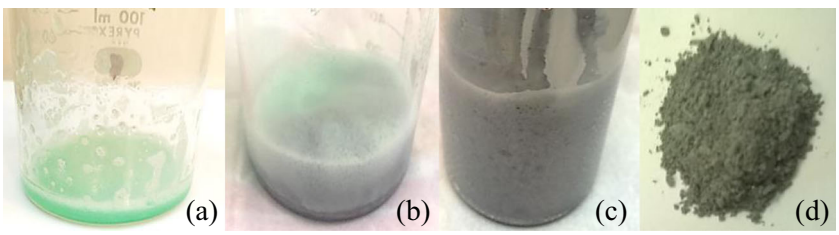

Fig. 2 Optical images for **a** nickel template mixture, **b** 2–3 min, **c** 15 min after addition of NaBH4 and **d** dry $Ni(OH)_2$-NF

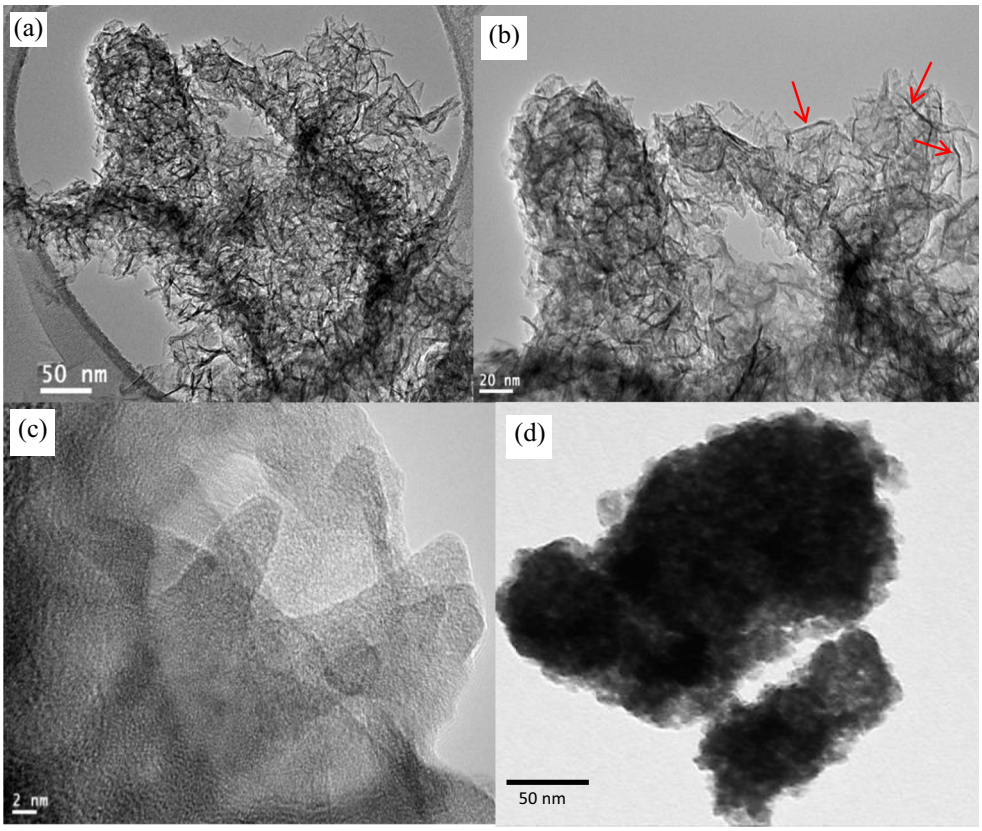

Fig. 3 TEM images of nickel hydroxide nanoflakes: **a** low, **b** and **c** high magnification and **d** TEM for bare nickel hydroxide deposited in the absence of surfactant

[30–33]. The XPS core level of O 1s region after deconvolution into three oxygen peaks is shown in Fig. 5c. The fitted peak at 530.6 eV can assign to the metal–oxygen bonds [34], and the peak at 531.4 eV is ascribed to the oxygen of OH groups [35, 36]. Moreover, the peak at 532.5 eV can be assigned to the multiplicity of adsorbed water near the surface [37].

The nitrogen adsorption–desorption isotherms of $Ni(OH)_2$-NF and bare-Ni are illustrated in Fig. 6a. The isotherm of $Ni(OH)_2$-NF (curve ii) exhibits typical type IV shape characteristic for mesoporous materials with sharp capillary condensation step at relative pressure (P/P^o) of 0.4–0.8. However, the isotherm shows hysteresis of H_2 type at high

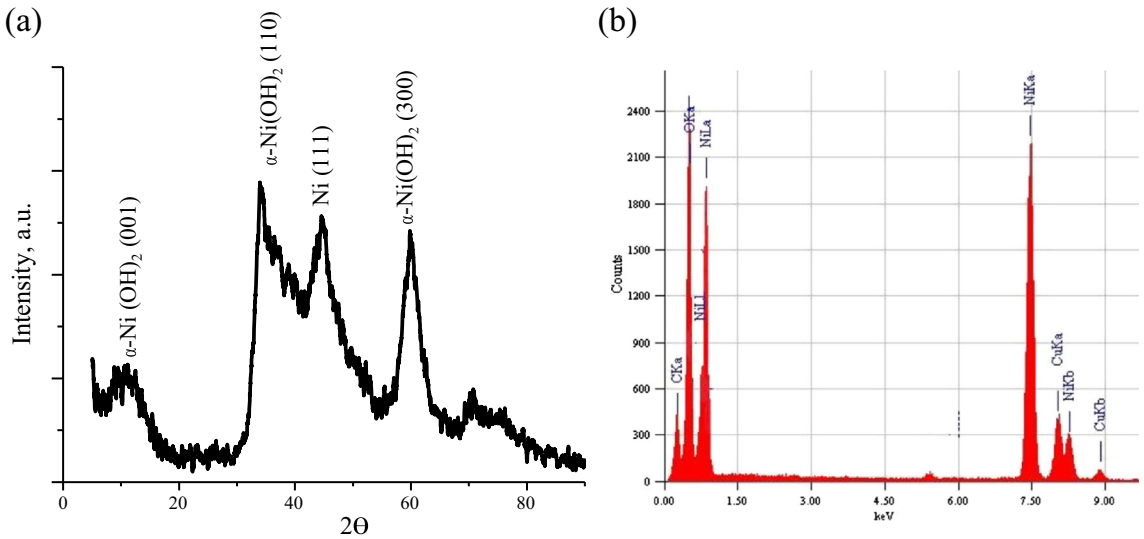

Fig. 4 **a** X-ray diffraction pattern and **b** EDX analysis of the produced $Ni(OH)_2$ nanoflakes

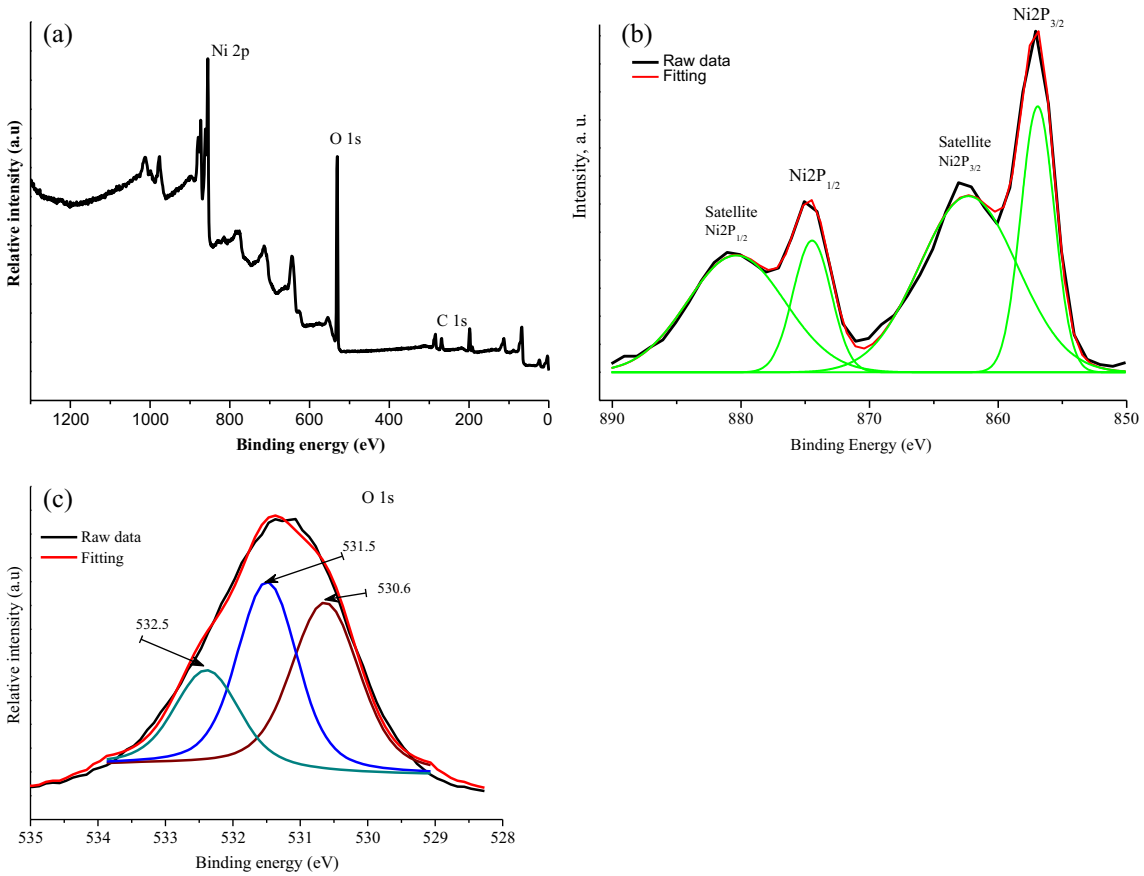

Fig. 5 **a** XPS survey spectra of $Ni(OH)_2$ nanoflakes, **b** high-resolution XPS spectra of Ni 2p and **c** O 1s core of $Ni(OH)_2$ nanoflakes

relative pressure that is due to disorder mesoporous structure [38]. The BET surface area of $Ni(OH)_2$-NF reaches 470 ± 5 m^2 g^{-1} which is significantly (20 times) higher than for bare-Ni (23 m^2 g^{-1}).

In addition, the total pore volume is equivalent to 0.525 and 0.04 cm^3 g^{-1} for $Ni(OH)_2$-NF and bare nickel, respectively, which indicate the successful formation of high surface area $Ni(OH)_2$ nanoflakes. Interestingly, the BET surface area of $Ni(OH)_2$-NF obtained here is more than two times higher than the value for $Ni(OH)_2$ nanosheets (190 m^2 g^{-1}) prepared by microwave-assisted deposition [19]. Also, it is about five times higher than the surface area of mesoporous $Ni(OH)_2$ (90 m^2 g^{-1}) obtained by using similar liquid crystal template by employing ethylenediamine borane as a reducing agent

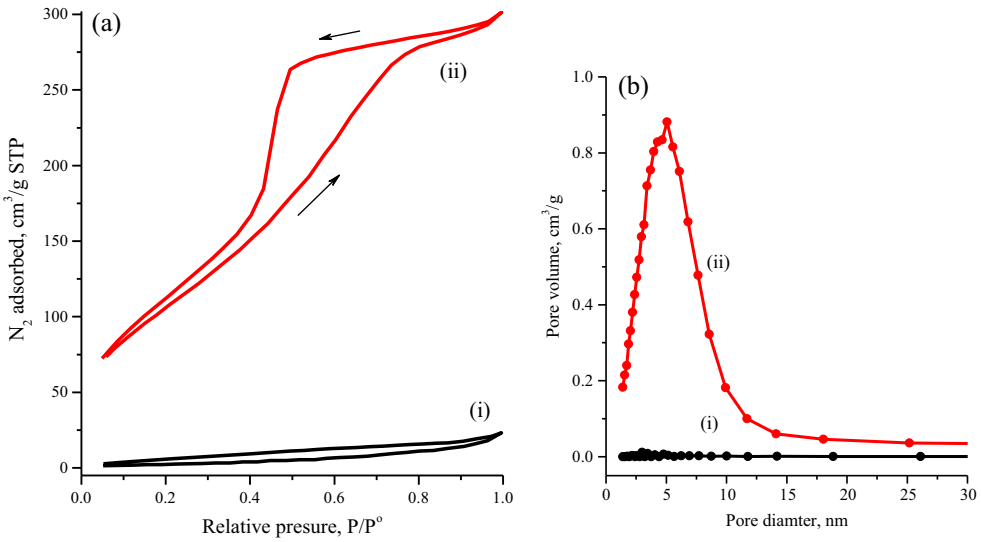

Fig. 6 **a** Nitrogen adsorption–desorption isotherm and **b** the corresponding BJH pore size distribution plot for bare-Ni (*i*) and $Ni(OH)_2$ nanoflakes (*ii*)

instead of $NaBH_4$ [29]. Such superior surface area proves that $Ni(OH)_2$ nanoflakes structure have a higher surface atom ratio that results from the harsh fragmentation of $Ni(OH)_2$ layers by dynamic hydrogen bubbles. The pore size distribution calculated by BJH method is in the range from 3 to 10 nm as shown in Fig. 6b. This wide range of pore size distribution can be related to the irregular inter-voids between the $Ni(OH)_2$ nanoflakes which formed due to the surfactant removal and the in situ hydrogen evolution which suggested that highly porous network structure is achieved. The pore size distribution analysis for bare-Ni (curve (i), Fig. 6b) shows flat line suggesting bulk deposit without any porous structure in nanometer range.

The electrochemical active surface area of $Ni(OH)_2$-NF and bare-Ni catalysts is firstly investigated by cyclic voltammetry (CV) is an alkaline solution. Figure 7 shows the CVs at 20 mV s^{-1} of glassy carbon electrode coated with the same amount (40 μg) of bare-Ni or $Ni(OH)_2$-NF ink in 1.0 M KOH solution in potential range from 0.0 to 0.7 V vs. SCE. Clearly, both electrodes show a couple of redox peaks aligned at about 0.37 V vs. SCE which correspond to the redox couple of Ni(II)/Ni(III) species [39, 40] according to Eq. (1).

$$Ni(OH)_2 + OH^- \rightarrow \alpha\text{–NiOOH} + H_2O + e^- \quad (1)$$

In comparison, the CV shows that the current of redox peaks for the $Ni(OH)_2$-NF catalyst is considerably higher (up to 10 times) than that for bare-Ni electrode. In addition for both $Ni(OH)_2$-NF and bare-Ni structures, no significant change was observed for the redox peaks' potential or for the difference between oxidation and reduction potentials ($\Delta E_p \cong 100$ mV) which confirms the similar electrochemical reaction (Eq. (1)) that takes place at both electrodes. The electroactive surface area (ESA) could be estimated by using the equation ($ESA = Q/(mq)$), where Q is the charge under the reduction peak of NiOOH to $Ni(OH)_2$, m is the mass loading and q is the charge required for a monolayer formation of $Ni(OH)_2$ which equals 257 μC cm^{-2} [41–43].

The obtained ESA for $Ni(OH)_2$-NF and bare-Ni electrodes equals to 154 and 13 cm^2 mg^{-1}, respectively. The achieved ESA of $Ni(OH)_2$-NF is significantly higher (about 11 times) than the ESA of bare-Ni as well as about two times higher than that for nickel nanowires (79 cm^2 mg^{-1}) as recently reported by Botte et al. [42]. Obviously, this confirms that $Ni(OH)_2$-NF catalyst possesses much higher electroactive surface area and roughness than bare-Ni due the formation of ultrathin nanoflakes.

Figure 8 shows a typical CV at 20 mV s^{-1} for $Ni(OH)_2$-NF electrode in the absence (curve (i)) and in the presence (curve (ii)) of 0.3 M urea in 1.0 M KOH. In the presence of 0.3 urea, the $Ni(OH)_2$-NF electrode shows a significant increase in the anodic current at the onset potential for the oxidation of Ni(II) to Ni(III) peak. At more positive potential, urea oxidation peak appears at 0.50 V vs. SCE followed by the oxygen evolution reaction at higher potentials. In addition, the reduction peak of Ni(II)/Ni(III) redox centre at 0.32 V vs. SCE during the reverse scan almost disappeared. Apparently, this significant enhancement in the anodic current and the simultaneous disappearance of the cathodic peak in the presence of urea are consistent with the behaviour of the catalytic regeneration EC mechanism [44].

Moreover, the ratio between urea oxidation peak current and the anodic peak current of Ni(II)/Ni(III) redox couple is more than five times demonstrating a strong electrocatalytic activity of $Ni(OH)_2$-NF electrode towards the oxidation of

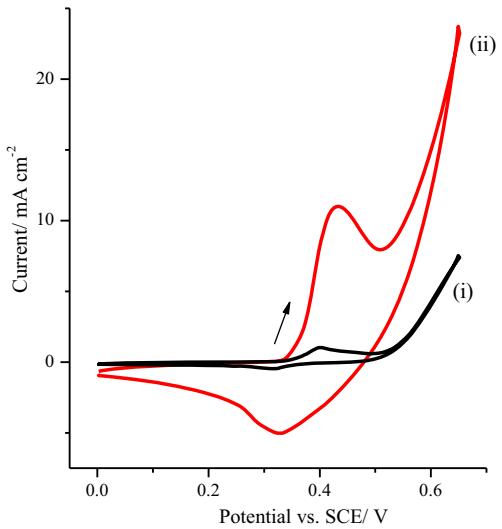

Fig. 7 Cyclic voltammetry at 20 mV s^{-1} for $Ni(OH)_2$-NF and bare-Ni electrodes in 1.0 M KOH: 40 μg of bare-Ni (*i*) and 40 μg $Ni(OH)_2$-NF (*ii*)

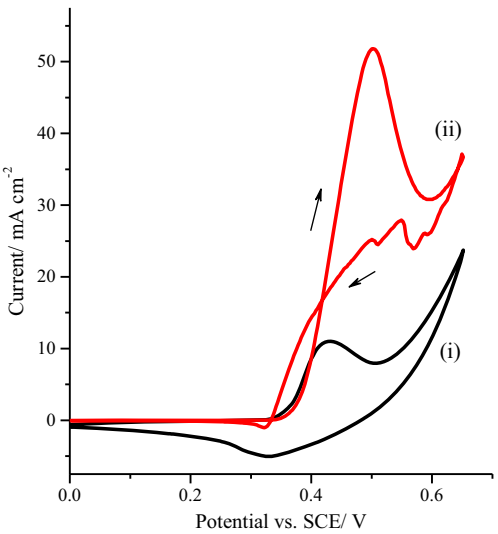

Fig. 8 Cyclic voltammetry at 20 mV s^{-1} for 40 μg $Ni(OH)_2$-NF electrode in the absence (*i*) and in the presence of 0.30 M urea in 1.0 M KOH (*ii*)

urea and the existence of electrocatalytic performance between urea and Ni(II)/Ni(III) active sites.

It is worth to note that the potential of oxygen evolution shifted to more positive potential in the existence of urea which may be due to the competing between urea oxidation and oxygen evolution reactions at the $Ni(OH)_2$-NF surface. This electrocatalytic EC mechanism is commonly observed for the electrochemical oxidation of small organic molecules such as methanol [45], ethanol [29] and glucose [46] when nickel-based catalyst is used in alkaline medium.

To investigate the effect of KOH concentration on urea oxidation, Fig. 9 shows the cyclic voltammetry at 20 mV s^{-1} of bare-GC, bare-Ni and $Ni(OH)_2$-NF electrodes in 0.3 M urea and 1.0 M or 5.0 M KOH solution. The bare-GC electrode (curve (i)) shows no current for the urea oxidation, indicating that the bare GC has no obvious electrocatalytic activity towards urea oxidation. In 1.0 M KOH solution, both bare-Ni (curve (ii)) and $Ni(OH)_2$-NF (curve (iii)) catalysts show the urea anodic oxidation peak at potential of 0.46 and 0.50 V vs. SCE, respectively.

Comparatively, $Ni(OH)_2$-NF catalyst exhibits significantly higher anodic current for urea oxidation than bare-Ni. For instance, urea oxidation currents (I_p) during the forward scan in 1.0 M KOH were determined as 12.5 and 51.8 mA cm^{-2} for bare-Ni and $Ni(OH)_2$-NF, respectively. A trivial shift (≅10 mV) in the onset potential of urea oxidation was observed at $Ni(OH)_2$-NF electrode suggesting that the nanoflakes have no influence on urea oxidation potential.

This enhancement in urea oxidation activity can be ascribed to the fact that $Ni(OH)_2$-NF catalyst has much higher electroactive surface area (154 cm^2 mg^{-1} than their bulk counterpart (13 cm^2 mg^{-1})) due to the presence of ultrathin nanoflakes structure, therefore more NiOOH active sites that promote the electron transfer and enhance the urea oxidation current. The electrooxidation of urea at $Ni(OH)_2$-NF electrode has also been studied in 5.0 M KOH in the presence of 0.3 M urea (Fig. 9, curve (iv)) under similar experimental conditions. The oxidation current of urea (I_p) during the forward scan was approximately 60 mA cm^{-2}, which is higher than in case of 1.0 M KOH. In addition, the onset potential of urea oxidation has significantly shifted to less positive potential (about 100 mV) showing that the urea oxidation reaction becomes thermodynamically more favourable at higher KOH concentrations. As reported by Botte et al. [47], the increase in urea oxidation current and negative shift of oxidation onset potential with increasing of KOH concentration can be related to the strong effect of OH^- ions on the formation of NiOOH species that subsequently catalyses the urea oxidation process. Also as shown in the inset in Fig. 9, when the KOH concentration has increased, further diminish in the reduction peak of NiOOH is observed in the presence of urea. This as reported in relevant works [48–50] related to more consumption of NiOOH during the oxidation of urea in concentrated KOH solution, and the urea electrooxidation reactions can be represented as below:

$$Ni(OH)_2(s) + OH^- \rightarrow \mathrm{NiOOH}\ (s) + H_2O\ (l) + e^- \quad (2)$$

$$\mathrm{NiOOH}\ (s) + CO(NH_2)_2(aq) \rightarrow \mathrm{Ni}(OH)_2(s) + \mathrm{product} \quad (3)$$

This EC reaction mechanism is confirmed by in situ surface-enhanced Raman spectroscopy, and the product of urea electrolysis was CO_2 and N_2 gas in alkaline media [44].

The concentration of urea has an effect on the performance of urea oxidation at nickel-based catalysts as reported by Botte et al. [47]. Here and as shown in Fig. 10a and in the inset, the urea oxidation peak current at $Ni(OH)_2$-NF electrode and

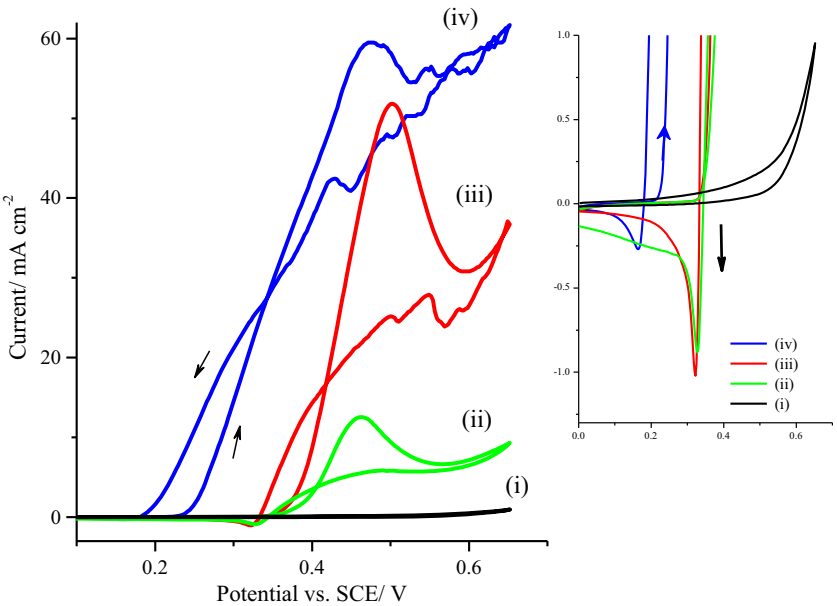

Fig. 9 Cyclic voltammetry at 20 mV s^{-1} for bare-GC (*i*), bare-Ni (*ii*) and $Ni(OH)_2$-NF electrodes (*iii*) in 0.3 M urea and 1.0 M KOH solution; $Ni(OH)_2$-NF electrode in 0.3 M urea and 5.0 M KOH solution (*iv*)

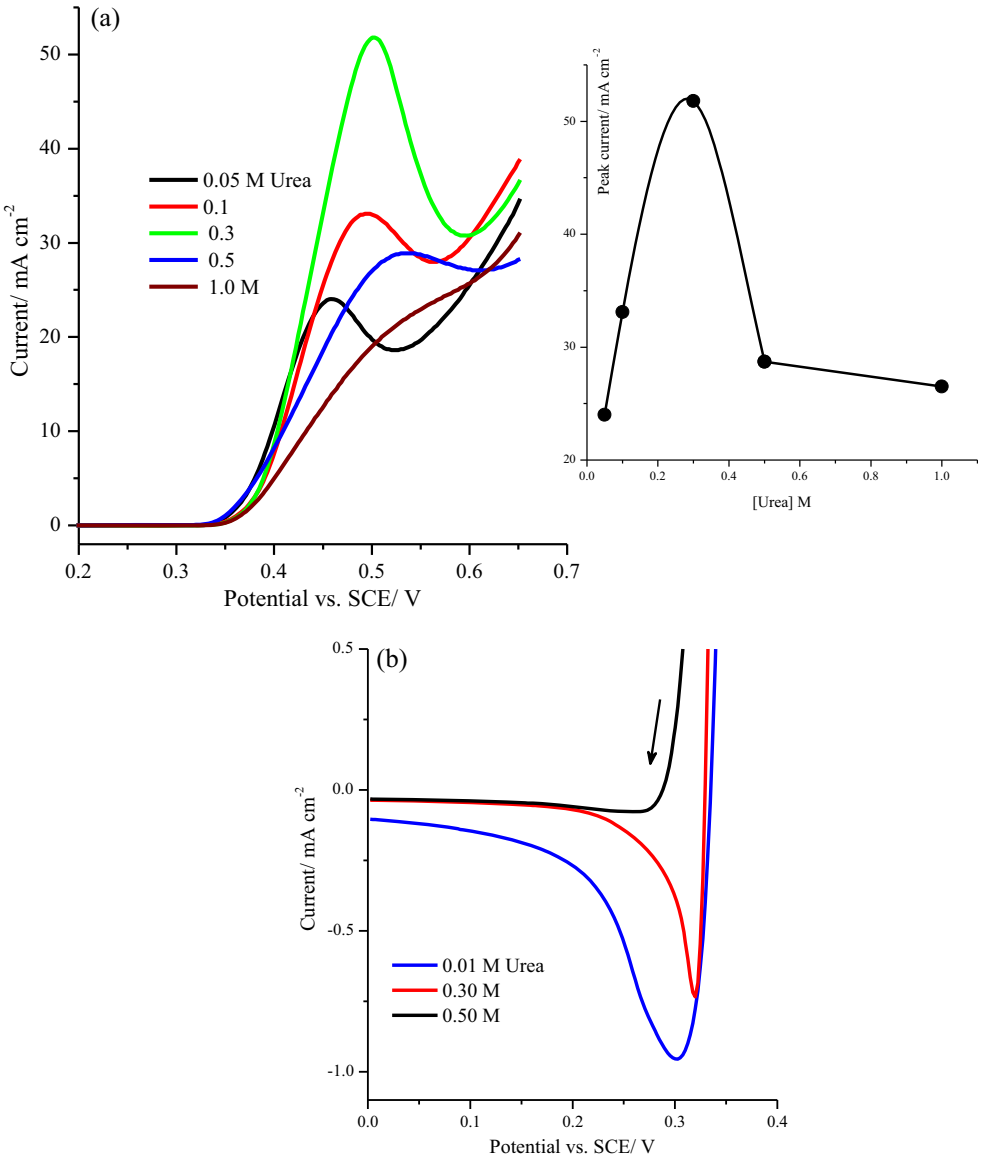

Fig. 10 Cyclic voltammetry at 20 mV s^{-1} for $Ni(OH)_2$-NF electrode in 1.0 M KOH and at different concentration of urea: **a** forward scan and **b** backward scan. The inset in **a** is the plot for the urea oxidation peak and urea concentration

during the forward scan increases linearly up to 0.3 M urea; then, the oxidation current drops at urea concentration higher than 0.3 M.

At urea concentrations below 0.3 M, the oxidation current increases linearly which attributed to the urea oxidation reaction that is under diffusion-controlled. On the other hand, at concentrations higher than 0.3 M, the oxidation current decreases because of more surface coverage of NiOOH active sites with urea and oxidation intermediate molecules than OH^- leading to rather more kinetic control reaction [47].

In addition, Fig. 10b shows the effect of increasing urea concentration on the disappearance of the Ni(III)/Ni(II) reduction peak at −0.3 V vs. SCE. Clearly, Fig. 10b shows the addition of more urea result in a gradual decrease in the Ni(III)/Ni(II) cathodic reduction peak current. This is because the urea oxidation at $Ni(OH)_2$-NF catalyst in alkaline solution follows the EC mechanism and increasing the urea concentration consumes more NiOOH and a decrease in reduction peak current and/or charge is observed.

For comparison of electrocatalytic activity of our $Ni(OH)_2$ nanoflakes with those similar nickel-based catalysts, Table 1 reports an evaluation of electrocatalytic mass activity and the experimental measurement conditions of $Ni(OH)_2$-NF and other related nickel-based catalyst studied in literatures [12, 41, 47–53].

Clearly, our $Ni(OH)_2$-NF catalyst is significantly more active (about 28 times higher with mass activity of 1295 A cm^{-2} g^{-1}) than that, for instance, nickel nanowire catalyst reported recently by Botte et al. [47] as catalyst mass activity of 46 A cm^{-2} g^{-1} was achieved for urea oxidation in KOH solution. Also, Botte et al. [12] reported 175 A cm^{-2} g^{-1} mass activity on $Ni(OH)_2$ nanosheet catalyst for urea oxidation in 5.0 M KOH solution which is considerably less effective than our $Ni(OH)_2$-NF catalyst. Moreover, $Ni(OH)_2$-

Table 1 Nickel-based catalyst mass activity measured in the presence of urea in 1.0 M KOH

Catalyst	Potential	Mass activity, A cm^{-2} g^{-1}	Reference
Nickel hydroxide nanoribbons	0.6 V vs. HgO	7.0 (a)	41
$Ni(OH)_2$ nanosheets	0.6 V vs. HgO	175(a)	12
Ni nanowires	0.6 V vs. HgO	46	47
$Ni(OH)_2$ nanocup arrays	0.5 V vs. SCE	100	52
$Ni(OH)_2$ hollow spheres		150	
$Ni(OH)_2$/Ni foam	0.5 V vs. SCE	400	53
$Ni(OH)_2$-NF/GCE	0.5 V (vs. SCE)	1295	This work

NF catalyst substantially showed better performance than $Ni(OH)_2$ nanosheets uniformly supported on highly porous nickel foam recently reported by Yang et al. [53] which recorded mass activity of 400 A cm^{-2} g^{-1}.

The electrocatalytic long-term activity and stability of $Ni(OH)_2$-NF catalyst towards urea oxidation in alkaline medium was examined by using potential multi-cycle voltammetry and chronoamperometry as shown in Fig. 11. The potential multi-cycle voltammetry in Fig. 11a shows cycle numbers 1 and 50 of $Ni(OH)_2$-NF electrode in 1.0 M KOH and 0.3 M urea at scan rate of 20 mV s^{-1}. The result of potential multi-cycles showed that the urea oxidation current at $Ni(OH)_2$-NF catalyst is almost stable and comparable CV is reproduced without deleterious or blocking effect up to 50 cycles. Though, after long cycling, the urea oxidation current is slightly reduced by about 10 %, apparently may be due to the physical detach of the catalyst from the GC electrode surface.

Figure 11b shows the chronoamperometry measurements at different constant potential for $Ni(OH)_2$-NF and bare-Ni electrodes that last for an hour in solution of 0.3 M urea and 1.0 M KOH. Initially, the current is quickly decreased at the beginning for all measurements due to double-layer charging.

Then, at both applied potential of 0.45 (curve (ii)) and 0.5 V vs. SCE (curve (iii)), the current time transients show that the steady-state current density for $Ni(OH)_2$-NF in the presence of 0.3 M urea is significantly greater than that for bare-Ni electrode (curve (i)) confirming the superior electrocatalytic activity of $Ni(OH)_2$-NF over bare-Ni electrode.

After running for 1 h at applied potential of 0.5 V vs. SCE, the steady-state current of the $Ni(OH)_2$-NF and bare-Ni electrodes is 22 and 2.1 mA cm^{-2}, respectively, which denotes that the $Ni(OH)_2$-NF electrode has excellent long-time electrocatalytic stability.

However, the current time transient shows the presence of current fluctuation at $Ni(OH)_2$-NF electrode at oxidation potential of 0.5 V (Fig. 11b, curve (iii)), which is presumably due to the evolution of N_2 and CO_2 gas result from the urea oxidation. Undoubtedly, the chronoamperometry measurement confirms that the $Ni(OH)_2$-NF catalyst is more active and stable for urea oxidation compared to the bare-Ni electrode which agrees well with the results obtained above by the CVs. After an hour of urea electrolysis, the steady-state mass activity at $Ni(OH)_2$-NF catalyst reaches 0.57 A cm^2 mg^{-1} which well exceeds for example the value of 0.33 A cm^2 mg^{-1} mass activity obtained by nickel hydroxide nanosheets supported on nickel foam catalyst [53]. This implies that the $Ni(OH)_2$-NF catalyst electrode exhibits superior activity and long-time electrocatalytic stability.

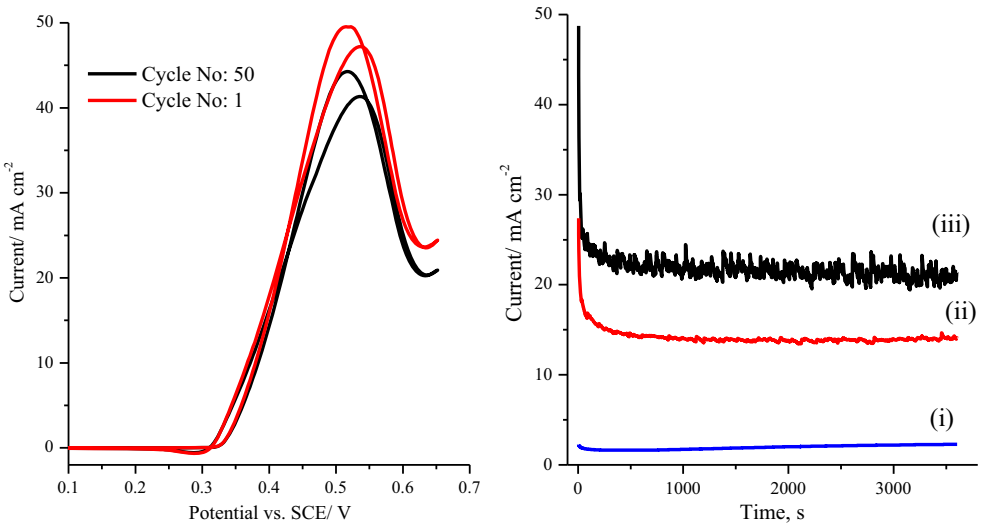

Fig. 11 **a** Cycle voltammetry (cycles 1 and 50) of $Ni(OH)_2$-NF electrode at scan rate of 20 mV s^{-1} in 1.0 M KOH and 0.3 M urea. **b** Current time transients during the oxidation of 0.3 M urea and 1.0 M KOH at bare-Ni at 0.5 V (*i*) and $Ni(OH)_2$-NF at potential at 0.450 V (*ii*) and 0.5 V vs. SCE (*iii*)

Conclusions

Ultrathin $Ni(OH)_2$-NF were successfully prepared via new approach of chemical reduction and exfoliation of nickel hydroxide layers confined in the aqueous domain of the hexagonal phase of Brij®78 surfactant template. Using excess of sodium borohydride reducing agent produces concurrent excessive dynamic hydrogen bubbles which exfoliate and fragment the nickel hydroxide layers precipitated within the soft hexagonal template. The physicochemical characterizations showed that the $Ni(OH)_2$-NF catalyst has high surface area of 470 m^2 g^{-1} which is significantly higher by a factor of 20 than that for bare nickel. The electrochemical measurements showed that the $Ni(OH)_2$ nanoflakes effectively enhanced the urea electrooxidation at a lower potential with superior mass activity over similar $Ni(OH)_2$-based nanostructures. Moreover, the chemical deposition and in situ exfoliation by using liquid crystal template and hydrogen dynamic bubbles offers a new inexpensive approach to nanostructuring and scale-up of a wide range of catalysts with enhanced catalytic performance.

Acknowledgments The authors would like to extend their sincere appreciation to the Deanship of Scientific Research at King Saud University for funding this research group no RG-1437-015.

References

1. J. R. Rostrup-Nielsen, J. Sehested, J. K. Norskov, *Hydrogen and Syngas by Steam Reforming,* (Academic Press, 2002).
2. S. Dunn, Int J Hydrog Energy **27**, 235-264 (2002)
3. C. Wu, L. Wang, P. T. Willians, J. Shi, J. Huang, Appl. Catal. B Environ. **108**, 6-13 (2011).
4. B. K. Boggs, R. L. King, G. G. Botte, Chem. Commun., 4859-4861 (2009).
5. W. Yan, D. Wang, G. G. Botte, Electrochim. Acta **61**, 25-30 (2012).
6. H. J. Bradley, Water Research **39**, 2245-2252 (2005)
7. C. C. Jara, S. Di Giulio, D. Fino, P. Spinelli, J Appl. Electrochem. **38**, 915-922 (2008).
8. A. N. Rollinson, J. Jones, V. Dupont, M. V. Twigg, Energy Environ. Sci. **4**, 1216-1224 (2011).
9. R. Y. Ji, D. S. Chan, J. J. Jow, M. S. Wu, Electrochem. Commun. **29**, 21-24 (2013).
10. A. Doner, E. Telli, G. Kardas, J Power Sources **205**, 71-79 (2012).
11. T. R. Ling, K. T. Lien, J. J. Jow, T. Y. Lin, Electroanalysis **21**, 2213-2219 (2009).
12. D. Wang, W. Yan, G. G. Botte, Electrochem. Commun. **13**, 1135-1138 (2011).
13. A. A. El-Shafei, J. Electroanal. Chem. **471**, 89-95 (1999).
14. A. T. Miller, B. L. Hassler, G. G. Botte, J. Appl. Electrochem. **42**, 925-934 (2012).
15. A. Chen, P. H. Hindle, Chem. Rev. **110**, 3767-3804 (2010).
16. A. Takagaki, C. Tagusagawa, S. Hayashi, M. Hara, K. Domen, Energy Environ Sci **3**, 82 (2010)
17. J. Liu, X. W. Liu, Adv. Mater. **24**, 4097-4111 (2012).
18. S. Guo, S. Dong, Chem. Soc. Rev. **40**, 2644-2672 (2011).
19. Y. Zhu, C. Cao, S. Tao, W. Chu, Z. Wu, Y. Li, Sci. Report **4**, 5787-7 (2014).
20. S. Ida, D. Shiga, M. Koinuma, Y. Matsumoto, J. Am. Chem. Soc. **130**, 14038-9 (2008)
21. C. Nethravathi, N. Ravishankar, C. Shivakumara, M. Rajamathi, J. Power Sources **172**, 970-974 (2007).
22. F. Song, X. Hu, Nature Commun. **5**, 4477-9 (2014).
23. H. Wang, H.-W. Lee, Y. Deng, Z. Lu, P.-C. Hsu, Y. Liu, D. Lin, Y. Cui, Nature Commun. **6**, 7261-8 (2015).
24. P. N. Bartlett, B. Gollas, S. Guerin, J. Marwan, Phys. Chem. Chem. Phys. **4**, 3835-3842 (2002).
25. P. A. Nelson, J. M. Elliott, G. S. Attard, J. R. Owen, Chem. Mater. **14**, 524–529 (2002).
26. Y. Yamauchi, T. Yokoshima, H. Mukaibo, M. Tezuka, T. Shigeno, T. Momma, T. Osaka, K. Kuroda, Chem. Lett. **33**, 542-543 (2004).
27. Y. Yamauchi, T. Momma, T. Yokoshima, K. Kuroda, T. Osaka, J. Mater. Chem. **15**, 1987-1994 (2005).
28. B. Li, M. Ai, Z. Xu, Chem. Commun. **46**, 6267-6269 (2010).
29. M. A. Ghanem, A. M. Al-Mayouf, J. P. Singh, T. Abiti, F. Marken, J. Electrochem. Soc. **162**, H453-H459 (2015).
30. M. C. Biesinger, B. P. Payne, L. W. M. Lau, A. Gerson, R. S. C. Smart, Surf. Interface Anal. 41, 324–332 (2009).
31. M. C. Biesinger, L. W. M. Lau, A. R. Gerson, R. S. C. Smart, Phys. Chem. Chem. Phys. **14**, 2434-2442 (2012).
32. J. W. Lee, T. Ahn, D. Soundararajan, J. M. Koc, J. Kim, Chem. Commun. **47**, 6305-6307 (2011).
33. D. S. Hall, D. J. Lockwood, C. Bock, B. R. MacDougall, Proc. R. Soc. **A 471**, 20140792 -65 (2015).
34. Z. Q. Liu, K. Xiao, Q. Z. Xu, N. Li, Y. Z. Su, H. J. Wang, S. Chen, RSC Adv. **4**, 43724380 (2013).
35. Y.-Z. Su, K. Xiao, N. Li, Z.-Q. Liu, S.-Z. Qiao, J. Mater. Chem. A **2**, 13845-13853 (2014).
36. C. M. Zhao, X. Wang, S. M. Wang, Y. Y. Wang, Y. X. Zhao, W. T. Zheng, Int. J. Hydrog. Energy **37**, 11846-11852 (2012).
37. Z. Q. Liu, Q. Z. Xu, J. Y. Wang, N. Li, S. H. Guo, Y. Z. Su, H. J. Wang, J. H. Zhang, S. Chen, Int. J. Hydrogen Energy **38**, 6657-6662 (2013).
38. IUPAC Recommendations, Pure Appl. Chem. **57**, 603-619 (1985).
39. M. A. Abdel Rahim, R. M. Abdel Hameed, M. W. Khalil, J. Power Sources **134**, 160-169 (2004).
40. M. Jafarian, M. Babaee, F. Gobal, M. G. Mahjani, J. Electroanal. Chem. **652**, 8-12 (2011).
41. D. Wang, W. Yan, S. H. Vijapur, G. G. Botte, J. Power Sources **217**, 498-502 (2012).
42. W. Yan, D. Wang, L. A. Diaz, G. G. Botte, Electrochim. Acta **134**, 266-271 (2014).
43. W. Yan, D. Wang, G. G. Botte, Appl. Catal. B Environ. **127**, 221-226 (2012).
44. V. Vedharathinam, G. G. Botte, Electrochim. Acta **108**, 660-665 (2013).
45. I. Danaee, M. Jafarian, F. Forouzandeh, F. Gobal, M. G. Mahjani, Int. J. Hydrog .Energy. **33**, 4367-4376 (2008).
46. Q. F. Yi, W. Huang, W. Q. Yu, L. Li, X. P. Liu, Electroanalysis **20**, 2016-2022 (2008).
47. V. Vedharathinam, G. G. Botte, Electrochim. Acta **81**, 292-300 (2012).
48. S. Majdi, A. Jabbari, H. Heli, J. Solid State Electrochem. **11**, 601-607 (2007).
49. H. Heli, M. Jafarian, M. G. Mahjani, F. Gobal, Electrochim. Acta **49**, 4999-5006 (2004).
50. M. Jafarian, F. Forouzandeh, I. Danaee, F. Gobal, M. G. Mahjani, J Solid State Electrochem. **13**, 1171-1179 (2009).
51. D. Wang, W. Yan, S. H. Vijapur, G. G. Botte, Electrochim. Acta **89**, 732-736 (2013).
52. M.-S. Wu, R.-Y. Ji, Y.-R. Zheng, Electrochim. Acta **144**, 194-199 (2014).
53. M.-S. Wu, G.-W. Lin, R.-S. Yang, J. Power Sources **272**, 711-718 (2014).